
This work was carried out in whole or in part within the framework of the NOMATEN Center of Excellence, supported from the European Union Horizon 2020 research and innovation programme (Grant Agreement No. 857470) and from the European Regional Development Fund via the Foundation for Polish Science International Research Agenda PLUS programme (Grant No. MAB PLUS/2018/8).

OPEN ACCESS
IOP Publishing
Modelling and Simulation in Materials Science and Engineering
Modelling Simul. Mater. Sci. Eng. **30** (2022) 085010 (15pp) https://doi.org/10.1088/1361-651X/ac9d54

# Dislocation nucleation mechanisms during nanoindentation of concentrated FeNiCr alloys: unveiling the effects of Cr through molecular simulations

**F J Dominguez-Gutierrez[1,*], A Ustrzycka[2], Q Q Xu[1], R Alvarez-Donado[1], S Papanikolaou[1] and M J Alava[1,3]**

[1] NOMATEN Centre of Excellence, National Centre for Nuclear Research, ul. A. Soltana 7, Otwock, Poland
[2] Institute of Fundamental Technological Research PAS, Pawinskiego 5B, Warsaw 02-106, Poland
[3] Department of Applied Physics, Aalto University, PO Box 11000, 00076 Aalto, Finland

E-mail: javier.dominguez@ncbj.gov.pl

Received 23 August 2022; revised 4 October 2022
Accepted for publication 25 October 2022
Published 4 November 2022

**Abstract**

Fe-based alloys with high chromium and nickel concentrations are very attractive for efficient energy production in extreme operating conditions. We perform molecular dynamics (MD) simulations of nanoindentation on fcc FeNiCr multicomponent materials. Equiatomic FeNi, $Fe_{55}Ni_{19}Cr_{26}$, and $Fe_{74}Ni_{8}Cr_{18}$ are tested by using established interatomic potentials and similar conditions, for the elucidation of key dislocation nucleation mechanisms and interactions. Generally, we find that the presence of Cr in these alloys reduces the mobility of prismatic dislocation loops, and increases their area, regardless of crystallographic orientation. Dislocation nucleation and evolution is tracked during mechanical testing as a function of nanoindentation strain and Kocks–Mecking continuum modeling displays good agreement with MD findings. Furthermore, the analysis of geometrically necessary dislocations (GNDs) is consistent with the Ma–Clarke's model at depths lower than 1.5 nm. The presence of Cr leads to a decrease of the GND density with respect to Cr-less FeNi samples, thus

* Author to whom any correspondence should be addressed.

Original Content from this work may be used under the terms of the Creative Commons Attribution 4.0 licence. Any further distribution of this work must maintain attribution to the author(s) and the title of the work, journal citation and DOI.

we find that Cr is critically responsible of increasing these alloys' hardness. Post-indentation impression maps indicate that Ni–Fe–Cr compositions display strain localization and hardening due to high Cr concentration.

Supplementary material for this article is available online

Keywords: nanoindentation, MD simulations, dislocation dynamics, continuum model, Ni alloys, Plasticity

(Some figures may appear in colour only in the online journal)

## 1. Introduction

Despite the high demand related to structural, mechanical and thermal properties' stability at reactor environment, concentrated FeNiCr alloys are considered as excellent candidates for applications at extreme conditions due to good corrosion resistance and thermodynamic stability [1–8]. It is understood that corrosion resistance in these materials is due to the presence of chromium ($\sim$20%) and high strength and ductility are maintained due to the inclusion of nickel [1, 9]. At the same time, fcc medium-entropy alloys synthesized with three different elements, e.g. FeNiCr, are of interest due to their industrial potential than high entropy alloys (HEAs) with more than four elements and traditional alloys, presenting phase stability over a wide range of temperatures and strain rates [10, 11]; along this line single solid solution alloys have been reported to present promising mechanical properties and to retain ductility and damage tolerance [10] due to lattice distortions or mismatches that more notorious than in conventional alloys [12].

Plasticity properties and deformation mechanisms may be unveiled through nanoindentation testing, that may provide information about hardness [2, 13–16] and overall plasticity mechanisms, in particular dislocation nucleation ones [1, 2, 17–22]. However, in nanoindentation testing, plasticity size effects are prevalent, masking mechanical properties, being the subject of vast experimental efforts [23–25]. Here, Nix and Gao [15] proposed a mathematical model for the size dependence of hardness, by considering the total density of dislocations separated into two densities of statistically stored dislocations (SSDs) and geometrically necessary dislocations (GNDs). The former constitutes a group of dislocations accumulated by multiplication during plastic deformation and the latter is accumulated in strain gradient fields caused by geometrical constraints. This is of interest in our work to describe at an atomic level the early stages of nanoindentation of concentrated FeNiCr alloys which is not possible to observe experimentally.

The major advantage of molecular dynamics (MD) simulations is the ability to investigate the thermomechanical stability of dislocation nucleation and defects' evolution [26–30]. Experimental exploration of material characterization needs to be supported by a computational and theoretical model where MD simulations have proven to be a powerful tool emulating experimental mechanical tests like nanoindentation [26–32]. Atomistic simulations can be further applied to study anisotropy in mechanical properties, providing a predictive tool for experiments with prohibitive technical limits and costs [33].

The present paper constitutes an attempt to fill in the gap related to multiscale computational modeling of mechanisms and plastic deformation of concentrated FeNiCr alloys by considering an equiatomic NiFe as a reference, as well as $Fe_{55}Ni_{19}Cr_{26}$ and $Fe_{74}Ni_8Cr_{18}$ alloys [34]. Thus, we present a detailed joint atomistic and continuum analysis of the plastic deformation mechanisms during nanoindentation, by taking into account the effects of crystallographic

**Table 1.** Size and atomic distribution of the numerical samples used to perform MD simulations.

| Orientation | Size (d$x$, d$y$, d$z$) (nm) | Atoms |
|---|---|---|
| [001] | (44.68, 43.97, 50.09) | 8 610 000 |
| [110] | (45.59, 44.83, 46.59) | 8 430 080 |
| [111] | (44.07, 43.62, 58.61) | 9 975 000 |

orientation and different percentages of Cr and Ni [5, 35]. Our manuscript is organized as follows: in section 2, we describe the computational methodology for carrying out single load nanoindentation tests where dislocations lines and dislocation loops nucleation mediates plastic deformation at early stages of the mechanical test. In section 3, we present results for the dislocation nucleation and interaction from MD simulations by introducing Kock–Mecking and Ma-Clarke's approaches in the discussion. Finally, in section 4, concluding remarks are summarized.

## 2. Methods

### *2.1. MD*

Atomistic computational modeling is based on the MD simulations by the Large-scale Atomic Molecular Massively Parallel Simulator (LAMMPS) [36] with interatomic potentials based on the embedded atom model (EAM) [34] to describe the atom-to-atom interactions in the FeNiCr samples. We start off by creating a pure fcc Fe sample with a lattice constant of 0.356 nm followed by randomly replacing Fe atoms by Ni and Cr atoms at [100], [110], and [111] crystal orientations where the numerical parameters that defined our numerical cells are presented in table 1. We consider three cases: equiatomic $Fe_{50}Ni_{50}$, $Fe_{55}Ni_{19}Cr_{26}$ and $Fe_{74}Ni_{8}Cr_{18}$ samples that are energy minimized to obtained the lattice distance mismatch for each sample. The obtained ones are then prepared by a series of Monte Carlo simulations to search for each possible metastable configuration at room temperature. Next, we applied a process of energy optimization and equilibration for 100 ps with a Langevin thermostat at 300 K and a time constant of 100 fs [30]. This is done until the system reaches a homogeneous sample temperature and pressure profile [28] with a density of $\sim$8.0 g cm$^{-3}$.

The computational dislocation nucleation model is an approximation to the roundness of the Berkovich and spherical tips into the consider errors due to the use of a spherical indenter in the MD simulations, which is limited to only few nm depths [37]. Furthermore, the 20 m s$^{-1}$ indentation speed considered in our work is smaller than the sound's speed in solids where our computational results can accurately capture the elastic Hertzian regime and provide information of early dislocation nucleation, similar to those obtained in experiments, along with a better understanding of the elastic–plastic deformation transition of the material. In figure 1, we present the initial frame of the nanoindentation simulation which is defined into three sections in the $z$ direction. Thus (a) the lowest bottom layers are kept frozen ($\sim 0.02 \times$ d$z$) to assure stability of the atoms when nanoindentation is performed; (b) a thermostatic region ($\sim 0.08 \times$ d$z$) above the frozen one is set to dissipate the generated heat during nanoindentation; and (c) the rest of the layers are defined as the dynamical atoms section, where the interaction with the indenter tip modifies the surface structure of the samples. Finally, a 5 nm vacuum section is added at the top of the sample [30, 31].

In our work, we use a microcanonical ensemble (NVE) to carry out the indentation test, where the velocity Verlet algorithm is implemented in LAMMPS with periodic boundary

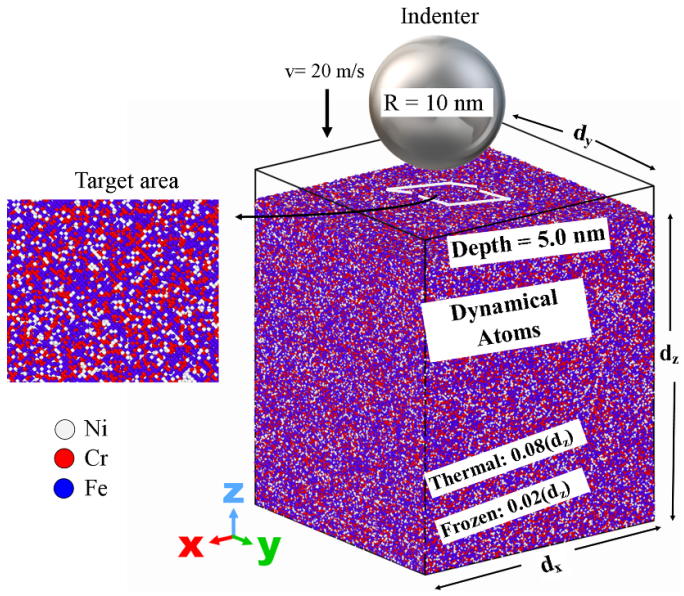


**Figure 1.** Schematic of the standard configuration in our MD simulations of nanoindentation. The prepared specimen is divided into three regions to consider boundary conditions and a non-atomic repulsive spherical indenter is used. Configuration of the target area shows the random atomic distribution of the sample.

conditions set on the $x$ and $y$ axes to simulate an infinite surface. A non-atomic repulsive imaginary rigid sphere defines our indenter tip as: $F(t) = K(r(t) - R)^2$ where the constant force is $K = 37.8$ MPa, and the trajectory of the center of the indenter tip is defined as $r(t) = (x_0, y_0, (z_0 \pm vt))$, with radius $R = 10$ nm, surface contact point as $x_0$ and $y_0$, and the initial gap $z_0 = 0.5$ nm between the surface and the intender tip to avoid effects of initial tip-surface interaction. The indenter tip's speed $v = 20\,\mathrm{m\,s^{-1}}$ is chosen as positive for loading, and as negative for unloading processes. Each calculation was performed for 125 ps with a time step of $\Delta t = 0.5$ fs for a maximum indentation depth of 4.0 nm to avoid the influence of boundary layers of the material. We consider the random atomic distribution of the elements on the material surface by performing $N_{\mathrm{MD}} = 10$ simulations at different indenter tip's positions into 10 nm $\times$ 10 nm target area, as depicted by a white square in figure 1. Thus, the load on the indenter $P$ is computed by the forces acting on the indenter in the $z$-axis direction and the depth $h$ is calculated as the displacement of the indenter tip relative to the initial surface of the material sample.

In order to obtain more information about the nanomechanical response during loading, we calculate the indentation stress and strain by considering the contact radius between the sample and the tip by using the geometrical relationship $a = \sqrt{R_i^2 - (R_i - h)^2}$. Thus, the nanoindentation stress and strain are calculated using the following equations [38]:

$$\sigma_{\mathrm{IT}} = \frac{P}{\pi a^2} \quad \text{and} \quad \epsilon = \frac{4h}{3\pi a} \tag{1}$$

where $P$ is load, $h$ is indenter displacement.

### *2.2. Analysis of dislocations nucleation and evolution*

We visualize and quantify different types of dislocations nucleated at different indentation depths by using the OVITO [39] software with the dislocation extraction algorithm [40]. Thus, we categorized the dislocations into several dislocation types according to their Burgers vectors as: $1/2\langle 110\rangle$ (Perfect), $1/6\langle 112\rangle$ (Shockley), $1/6\langle 110\rangle$ (Stair-rod), $1/3\langle 100\rangle$ (Hirth), $1/3\langle 111\rangle$ (Frank). Thus, we compute the dislocation density, $\rho$, as a function of the depth by using the approximation of a spherical plastic zone as

$$\rho = \frac{3N_{\mathrm{D}}l_{\mathrm{D}}}{2\pi(R_{\mathrm{pl}}^3 - h^3)}, \tag{2}$$

where $N_{\mathrm{D}}$ is the number of dislocations measured during nanoindentation test; $l_{\mathrm{D}}$ is the dislocation length of each type, and $R_{\mathrm{pl}}$ is the largest distance of a dislocation measured from the indentation displacement, considering a hemispherical geometry.

Continuum modeling [41] is applied to the MD results for the dislocation density as a function of the indentation strain to describe the materials hardening due to the storage of dislocations induced by plastic strain as [42]

$$\frac{\mathrm{d}\rho}{\mathrm{d}\gamma} = M\left(\frac{\mathrm{d}\rho}{\mathrm{d}\gamma}\Big|_{+} + \frac{\mathrm{d}\rho}{\mathrm{d}\gamma}\Big|_{-}\right). \tag{3}$$

The dislocation motion accounts for plastic deformation and therefore ductility. The evolution of the total dislocation density $\rho$ during plastic deformation is decomposed into the component of dislocation multiplication denoted by $(+)$ associated with the production of new dislocations and the annihilation component denoted by $(-)$. Dislocation annihilation proceeds as the result of a process known as dynamic recovery. The annihilation mechanism evolves with a large deformation, in which immobile dislocations are released to cancel out immediately with neighbors of opposite signs. Together with dislocation generation, the mechanism of annihilation is responsible for the saturation level of the dislocation densities to at large strain. As a result the relationship between the evolution of dislocation densities and the plastic strain is obtained in the following form

$$\frac{\mathrm{d}\rho}{\mathrm{d}\gamma} = \left(\frac{k}{b}\sqrt{\rho} - k_{\mathrm{a}}\rho\right) \tag{4}$$

where $b$ denotes the Burgers vector magnitude, $\gamma$ denotes the plastic shear, $k$ is a constant for the dislocation accumulation due to the interaction with forest dislocations as obstacles, and $k_{\mathrm{a}}$ is the dislocation annihilation constant due to dynamics recovery [43]. The relation between the effective plastic strain rate $\dot{\epsilon}$ and the plastic shear $\dot{\gamma}$ is expressed by a mean orientation factor $M$ as $\dot{\gamma} = \dot{\epsilon}M$.

## 3. Results

### *3.1. Load-depth curves*

We compare all studied cases on equal grounds, towards identifying effects of Cr concentration variability. In figure 2, we show results for the load displacement (LD) curves for the three samples at three different crystal orientations to investigate their effects on the mechanical properties of the materials. One can observe that the pop-in event guides the elastic–plastic transition which is observed as a deviation of the force respect to the Hertz fitting curve defined as [22, 44]: $P_{\mathrm{H}} = 4/3E_{\mathrm{H}}R^{1/2}h^{3/2}$ that is calculated as the effective elastic modulus $E_{\mathrm{H}}$ of the studied system [45]. For all studied compositions, one may notice that the maximum (across

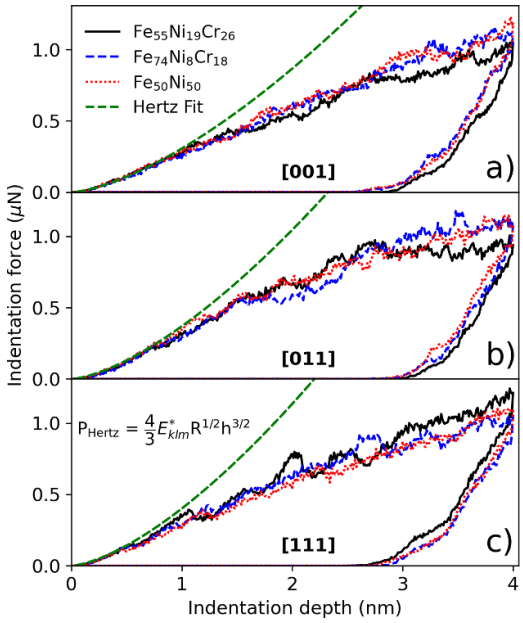


**Figure 2.** LD curve obtained from the numerical modeling on the main crystal orientation: [001] in (a), [011] in (b), and [111] in (c). Pop-in event identification is done by comparing to Hertz fitting curve.

cases) pop-in load is observed for the [001] orientation at ∼1 nm, followed by [011] and [111] orientations, something typical of fcc crystals regardless of the chemical composition [30, 32]. Furthermore, the comparison among cases, shows that the Cr concentration leads to a noticeable effect on the overall response and hardness, that increases with Cr. However, the details of the overall effect of high Cr concentration shall be investigated experimentally for the mechanical properties of these materials.

The comparison among cases becomes clearer when the load-depth curves are transformed to nanoindentation stress–strain ones [38]. Figure 3 reports the nanoindentation stress as a function of the strain by using equation (1) as an attempt to correlated to results reported by uniaxial compression test. We notice a shift of the elastic part of the nanoindentation test respect to the Hertz fitting curve and the yield point is located into a strain range of 0.21%–0.2% depending on the crystal orientation. It is also observed that the stress decreases significantly after a strain of 0.5% for the [011] orientation, regardless the chemical composition. This is due to the fcc geometry of the sample and the expected nucleation of prismatic dislocation loops (PDLs) on the direction of the applied indentation tip.

### *3.2. MD and continuum modeling*

A comparison of the evolution of the dislocation density for different crystal orientations and chemical compositions, as a function of the indentation strain obtained from MD simulations with theoretical curve (equation (4)) is shown in figure 4. The agreement can be regarded as satisfactory by considering the removal of the elastic region in the comparison that is defined by the pop–in event in figure 3. This also shows that the adopted constitutive assumptions (equation (4)) are sufficient for the description of kinetics of dislocation density. This equation

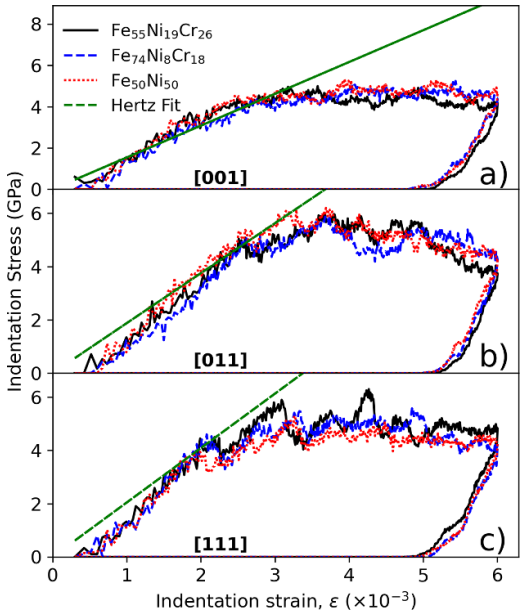


**Figure 3.** Average of indentation stress as a function strain at [001] in (a), [011] in (b), and [111] in (c) crystal orientation.

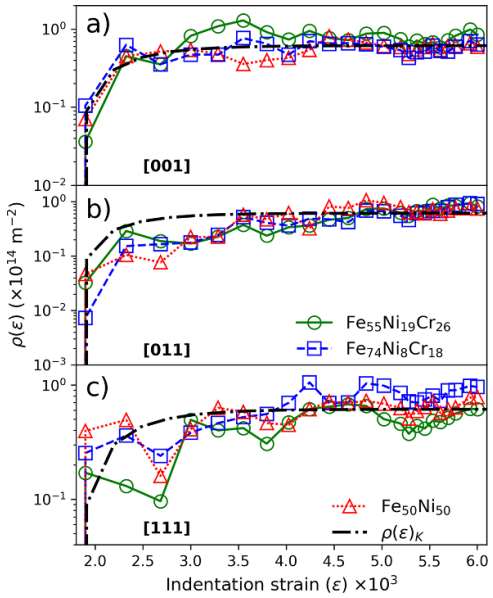


**Figure 4.** Dislocation density as a function of the indentation strain at different crystal orientation for [001] in (a), [011] in (b), and [111] in (c). Considering different concentration of Ni and Cr. Comparison between MD results and continuum model was done by considering the plastic region.

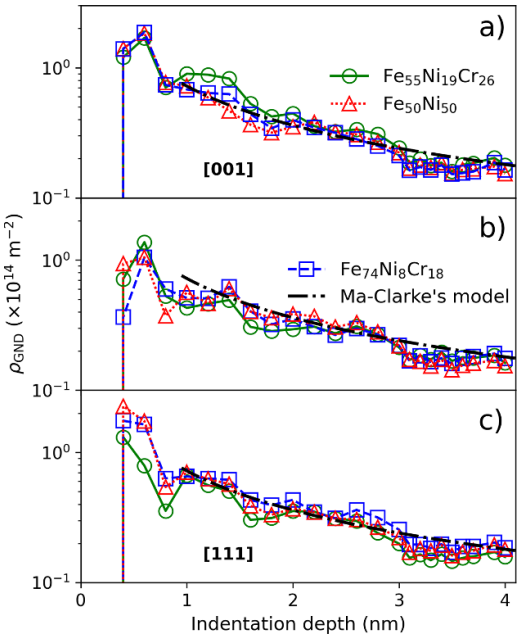


**Figure 5.** GND density, $\rho_{GND}$, as a function of the depth by MD simulations with Ma–Clarke's model, showing a good agreement to the plastic region.

is assumed to principally reflect the dislocation mechanisms governing inelastic deformation in the indented material where early stages of nanoindentation test are highly dependent on the crystal orientation as shown by results less than 0.003 strain. We also noticed that the oscillations presented by dislocation density from MD can be associated to the nucleation of PDLs, that cannot be identified by the continuum modeling.

During loading process in nanoindentation test, it is of interested to understand the effects of different concentrations of Cr and arrangements on the materials' surface on the dynamics of GND nucleated into the plastic region underneath the tip. In general, the GND density has to be directly related to the strain gradient as follows:

$$\rho_{\mathrm{GND}} = \frac{4\gamma}{bl} \tag{5}$$

where $\gamma$ is the shear applied on the primary slip plane and $l$ is defined as some finite length connected with the particle size. For a rough estimate of the geometrically stored dislocations GNDs, Ma and Clarke [46] proposed the average shear strain, $\gamma_{\mathrm{avg}}$, below the indenter tip as

$$\rho^{\mathrm{NI}}_{\mathrm{GND}}(h) = \frac{4\gamma_{\mathrm{avg}}}{bD(h)} \tag{6}$$

where $D$ is here considered as the size of the contact area during the loading process (as a function of the depth, $h$), $\gamma_{\mathrm{ave}}$ is a fitting parameter to the MD results in our work, as reported in figure 5. It is assume that the $\gamma_{\mathrm{avg}}$ remained constant throughout penetration. In general, the extended Nye-tensor method reported by Begau *et al* [47] and applied to compute the GNDs density from MD simulations concludes that $\rho^{\mathrm{MD}}_{\mathrm{GND}} \approx 0.1\rho^{\mathrm{MD}}_{\mathrm{Tot.}}$ in fcc crystals, where $\rho^{\mathrm{MD}}_{\mathrm{Tot.}}$ is the total dislocation density; obtained by equation (5). In figure 7, we report GND

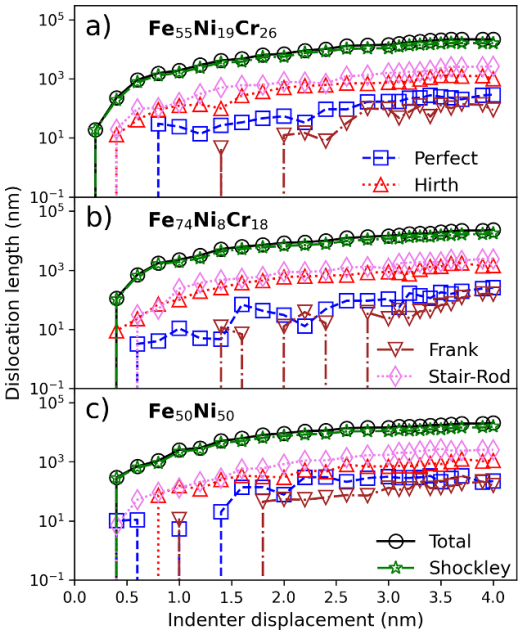


**Figure 6.** Length of dislocations nucleated during loading process for $Fe_{55}Ni_{19}Cr_{26}$ in (a), $Fe_{74}Ni_8Cr_{18}$ in (b), and equiatomic FeNi in (c) on the [011] crystal orientation.

density as a function of indentation depth as $0.1\rho_{Tot}^{MD}$ noting that results follow the Ma and Clarke relationship where crystallographic orientations effects are observed at the beginning of the indentation test. We have also noted that GNDs created in the volume deformed by the indentation are directly related to lattice distortion which suggests that the production of GNDs has a considerably key role on strength of FeNiCr multicomponent alloys; where the presence of multi-elements makes slip paths of dislocations differently shaped than for single element metals [31]. Also, a satisfactory agreement between the Ma–Clarke model and the MD results is presented after 1 nm depth, regardless the crystal orientation and chemical complexity due to the fcc structure of the alloys.

### *3.3. Dislocation nucleation effects*

The effects on hardness can be further elucidated through the investigation of dislocation dynamics during nanoindentation. In figure 6 we show results of the average length of dislocations nucleated during loading process of the three samples on the [011] crystal orientation where single PDLs are mainly nucleated. Results for [001] and [111] orientations are included in the supplementary material (SM) section. In general, it is noted that Frank and perfect type of dislocations are mainly affected by the chemical composition of the samples at indentation depths less than 2 nm. It is also observed that Hirth and Stair-rod type dislocation are present during the loading process due to the dissociating of 1/6 $\langle 112 \rangle$ dislocations. Thus, the interaction of symmetrical Shockley dislocations are suggested to be responsible for PDLs nucleation, for different crystal orientations [31].

In figure 7, we show the dislocation lines and loops nucleated at 1 nm, 4 nm depth that is considered as the maximum indentation penetration, and after unloading process where the

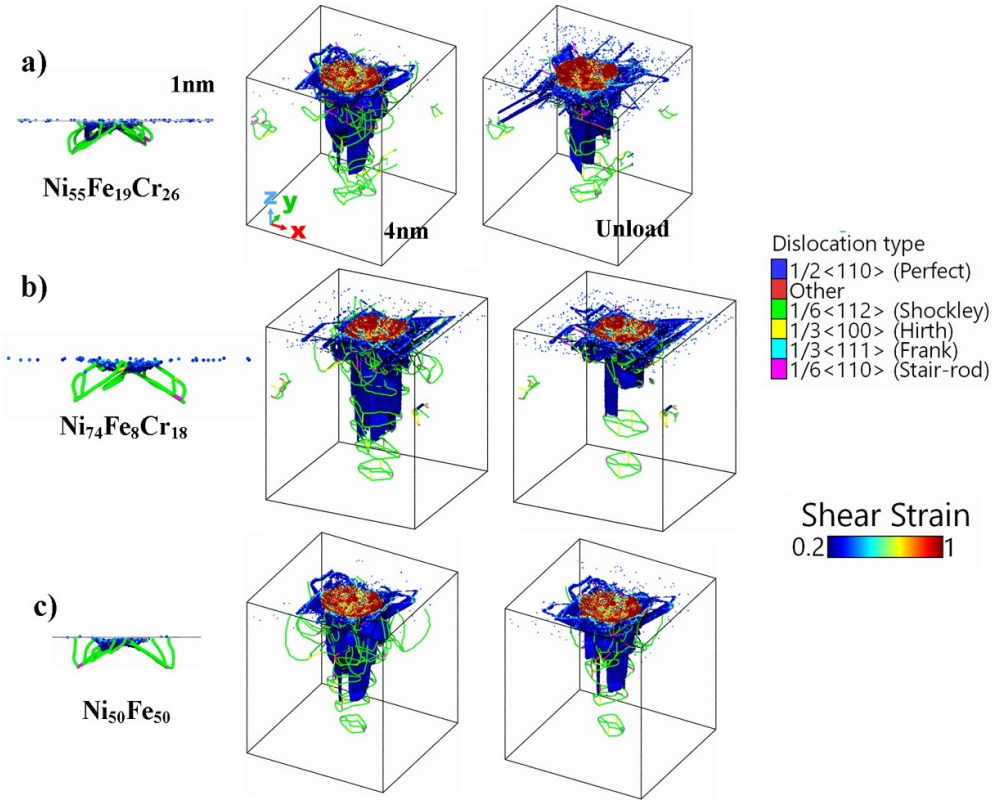


**Figure 7.** Dislocations nucleated during the loading process at 1 nm, 4 nm (max. depth) and after unloading process for the $Fe_{55}Ni_{19}Cr_{26}$ in (a), $Fe_{74}Ni_8Cr_{18}$ in (b), and equiatomic FeNi in (c) on the [011] crystal orientation. Atomic shear strain mapping is included to indicate the relation between dislocation nucleation and strain. The dislocation types are colored according to their Burgers vectors as: $1/2\langle 110\rangle$ Perfect (blue), $1/6\langle 112\rangle$ Shockley (green), $1/6\langle 110\rangle$ Stair-rod (red), $1/3\langle 100\rangle$ Hirth (yellow), $1/3\langle 111\rangle$ Frank (turquoise).

indenter tip is fully removed for the $Fe_{55}Ni_{19}Cr_{26}$ in (a), $Fe_{74}Ni_8Cr_{18}$ in (b), and equiatomic FeNi in (c). The calculations were carried out for a particular MD simulation on the [011] crystal orientations and an atomic shear strain mapping is included in the figure; noticing a relation between shear strain and dislocation propagation. Atoms with shear strain values lower than 0.2 were removed from the figure. We noticed that the dislocation loops follow the {111} slips system where PDLs are found due to the interaction of Shockley type dislocation during the loading process. The formation of stacking fault tetrahedron (SFT) is not observed for the [011] and [111] orientations. However, obtained numerical results shows that the dynamics of PDLs on the [001] crystal orientation tend to form SFT due to the $1/3\langle 100\rangle$ Hirth dislocation junction by the interaction of Shockley type dislocations, as presented in the SM. On the [011] orientation, we observe the propagation of PDL through the sample where four loops were found at the maximum depth. After the unloading process, two PDLs are pushed back and they are absorbed by the surface, leaving two PDLs in the sample after the nanoindentation test.

**Table 2.** Prismatic dislocation loop (PDL) sizes for equiatomic FeNi, $Fe_{55}Ni_{19}Cr_{26}$, and $Fe_{74}Ni_8Cr_{18}$ at the maximum indentation depth for different crystal orientations. Total length (TL) of the PDL is obtained as: Shockley + Stair-rod + Hirth lines in units of (nm); and total area as: minor diagonal × major diagonal in units of $nm^2$, as reported in our previous work [31].

| | [001] | | [011] | | [111] | |
|---|---|---|---|---|---|---|
| PDL | Area | TL | Area | TL | Area | TL |
| | | | FeNi | | | |
| 1 | 83.34 | 46.03 | 44.70 | 54.48 | 140.66 | 57.68 |
| 2 | 91.12 | 47.04 | 67.35 | 70.03 | 80.95 | 44.42 |
| 3 | 91.30 | 48.03 | 96.71 | 46.50 | 53.13 | 35.11 |
| 4 | 23.32 | 26.91 | — | — | 31.19 | 25.22 |
| | | | $Fe_{55}Ni_{19}Cr_{26}$ | | | |
| 1 | 111.68 | 48.91 | 55.22 | 34.08 | 156.9 | 59.44 |
| 2 | 89.98 | 47.71 | 89.07 | 46.64 | 68.46 | 37.10 |
| 3 | — | — | 44.21 | 36.63 | 107.68 | 49.08 |
| 4 | — | — | 91.26 | 45.65 | — | — |
| | | | $Fe_{74}Ni_8Cr_{18}$ | | | |
| 1 | 101.2 | 50.92 | 47.77 | 34.87 | 76.77 | 44.05 |
| 2 | 142.9 | 57.21 | 74.24 | 42.53 | 36.07 | 27.06 |
| 3 | — | — | 61.57 | 40.84 | — | — |
| 4 | — | — | 159.49 | 59.28 | — | — |
| 5 | — | — | 33.48 | 31.87 | — | — |

Several defects in the materials can be nucleated during loading process where dislocation partials and junctions can lead to the nucleation of PDLs mainly formed by Shockley type and more complex defects like pyramidal shaped STF that are nucleated from PDLs and defined by Hirth junctions, as reported for nanoindentation and irradiation induced defects in fcc concentrated solid solution alloys [31, 48]. In order to characterize the effects of Cr concentration on the nanostructure of FeNiCr alloys, we track nanoindentation induced defects nucleation by calculating the area and total length of the PDL at the maximum indentation depth, as reported in table 2.

We noticed formation of pyramidal shaped SFT on the [001] orientation for all the samples due to the interaction of PDLs, which shows the effects of crystallographic orientation on the nanoindentation induced defects nucleation. Besides, the different concentrations of Cr and Ni in the Fe-based alloys tends to slow down the mobility of nucleated PDL which decreases the number of SFT in the samples for this crystal orientation. For the [111] orientation, the number of PDL also decreases respect to FeNi sample, where low concentration of Ni influences the nucleation of PDLs and their mobility. No SFT where observed for this specific crystal orientation. Finally, for the [011] orientation the nucleation and mobility of PDLs are affected by the chemical composition of the materials. For equiatomic FeNi sample, we did not observe complete PDLs during loading process Where the number of loops can be observed by adding Cr to the sample and varying the concentration of Ni.

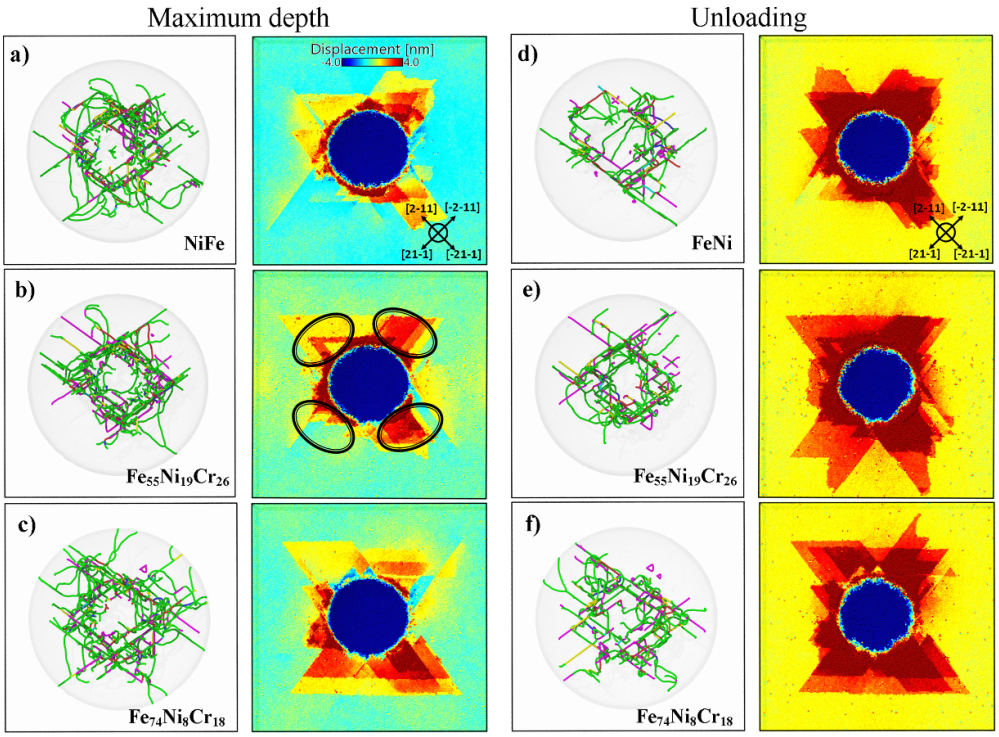


**Figure 8.** GND visualization and pile-ups formation by MD simulation for the maximum indentation depth in (a)–(c) and after removing the indenter tip (d)–(f) on the [110] orientation; plastic volume is depicted by a gray colored sphere. Dislocation types are colored according to their Burgers vectors following the color palette used in figure 8.

### *3.4. Post-indentation maps*

In figure 8 we present the atomic displacement for the [011] orientation at the maximum indentation depth (figures 8(a)–(c)) and after nanoindentation test (figures 8(d)–(f)), respectively. Besides, the visualization of the GNDs nucleated at the maximum indentation depth and after nanoindentation test, a gray circle is added to the plastic deformation volume due to the fact, that the plastic area around the indent is proportional to four up to ten times of the indentation depth [17]; the GNDs analysis was provided from the larger area. These images show the fourfold symmetry and the attainment of crystallographic slip directions on the {211} and symmetric planes that are observed for the [011] crystal orientation [29, 49] in fcc materials. Also, our simulation take into account the nanomechanical response of the materials by removing the indenter tip, where the elastic recovery favors (a) upward dislocation glide, (b) dislocation surface annihilation, and (c) the onset of further surface decorations (figure 8). Here, the slip trace patterning and its development become more evident during unloading which leads to an enhancement of the topographical features that were not clear in the loading indentation. Being modified by the presence of Cr in the FeNi alloys that, at some extended, can be qualitatively compared to experimental SEM observations into the limitation of the modeling by the EAM interatomic potentials. Results for [001] and [111] orientations are reported in the SM of this manuscript.

The chemical composition and the high Cr concentration in the materials affect the nucleation of the GNDs as observed in figure 8 and the recovery of the material after removing the indenter tip; where the accumulation rate of GNDs can be described by the geometric slip distance, parameter strongly dependent on the microstructure and independent of shear strain [50]; as presented by the formation of pile-ups for different materials. The geometric slip distance is analogous to the slip distance for the SSDs and expresses the effectiveness of particles or grain in causing dislocations to be stored.

## 4. Concluding remarks

In this work, we presented an atomistic-based computational investigation of the nanomechanical responses of concentrated fcc NiFeCr alloys: equiatomic NiFe as a reference, $Fe_{55}Ni_{19}Cr_{26}$ and $Fe_{74}Ni_8Cr_{18}$. We described dislocation nucleation mechanisms and dislocation evolution at different crystal orientations in terms of their high Cr concentration dependence. The characterization of the nanoindentation process is done through tracking dislocation dynamics and densities at different indentation depths. In addition, pyramidal shaped SFT defects are formed due to the interaction of PDLs and observed only for the [001] orientation. The analysis of the nanoscale elastic–plastic behavior of these alloys using nanoindentation, as well as pile-up patterns and atomic strains distribution using MD simulations, shows a strong dependence on Cr concentration; the fitting of load-depth and dislocation density curves based on Kocks–Mecking phenomenology, as a function of the indentation strain, shows agreement with common hardening plasticity mechanisms; the use of the Ma–Clarke model for describing GNDs density as a function of indentation depth is in good agreement with the MD results; finally, high concentration of Cr in the alloys reduces the mobility of PDLs and increases their size, independently of crystal orientation. We believe our computational study may inspire the design of more advanced chemically complex functional materials and understand their mechanical properties at operating conditions of future advanced nuclear reactors.

## Data availability statement

All data that support the findings of this study are included within the article (and any supplementary files).

## Acknowledgments

We would like to thank Professor Lukasz Kurpaska for fruitful experimental discussions related to nanoindentation tests. We acknowledge support from the European Union Horizon 2020 research and innovation program under Grant Agreement No. 857470 and from the European Regional Development Fund via the Foundation for Polish Science International Research Agenda PLUS program Grant No. MAB PLUS/2018/8 (R A D, S P, and M J A). This work has been partially supported by the National Science Centre through the Grant No. UMO-2020/38/E/ST8/00453 (F J D G and A U). We acknowledge the computational resources provided by the High Performance Cluster at the National Centre for Nuclear Research in Poland, as well as the support of the Interdisciplinary Centre for Mathematical and Computational Modelling (ICM) University of Warsaw under computational allocation No. g88-1181.

## ORCID iD

F J Dominguez-Gutierrez https://orcid.org/0000-0002-1429-0083

## References

[1] Lo K, Shek C and Lai J 2009 *Mater. Sci. Eng.* R **65** 39–104
[2] Chen T, Tan L, Lu Z and Xu H 2017 *Acta Mater.* **138** 83–91
[3] Wen D, Jiang B, Wang Q, Yu F, Li X, Tang R, Zhang R, Chen G and Dong C 2017 *Mater. Des.* **128** 34–46
[4] Isakov M, May M, Hiermaier S and Kuokkala V T 2016 *Mater. Des.* **106** 258–72
[5] Zhang X, Li D, Li Y and Lu S 2019 *Mater. Sci. Eng.* A **743** 648–55
[6] Wróbel J S, Nguyen-Manh D, Lavrentiev M Y, Muzyk M and Dudarev S L 2015 *Phys. Rev.* B **91** 024108
[7] Szuwalski K and Ustrzycka A 2012 *Int. J. Non-Linear Mech.* **826** 141912
[8] Szuwalski K and Ustrzycka A 2013 *Eur. J. Mech.* A **27** 79–85
[9] Liu Z, He Y and Gao W 1997 *J. Mater. Eng. Perform.* **7** 88–92
[10] Yeh J W, Chen S K, Lin S J, Gan J Y, Chin T S, Shun T T, Tsau C H and Chang S Y 2004 *Adv. Eng. Mater.* **6** 299–303
[11] Miracle D and Senkov O 2017 *Acta Mater.* **122** 448–511
[12] Wang Z, Huang Y, Yang Y, Wang J and Liu C 2015 *Scr. Mater.* **94** 28–31
[13] Xia W, Dehm G and Brinckmann S 2019 *Mater. Des.* **183** 108169
[14] Schuh C A 2006 *Mater. Today* **9** 32–40
[15] Nix W and Gao H 1998 *J. Mech. Phys. Solids* **46** 411–25
[16] Oliver W and Pharr G 1992 *J. Mater. Res.* **7** 1564–83
[17] Mattucci M, Cherubin I, Changizian P, Skippon T and Daymond M 2021 *Acta Mater.* **207** 116702
[18] Cui L, Jiang S, Xu J, Peng R L, Mousavian R T and Moverare J 2020 *Mater. Des.* **198** 109385
[19] Zhang T Y, Xu W H and Zhao M H 2004 *Acta Mater.* **52** 57–68
[20] Zhang F, Huang Y and Hwang K C 2006 *Acta Mater.* **22** 1–8
[21] Rodriguez R and Gutierrez I 2003 *Mater. Sci. Eng.* A **361** 377–84
[22] Papanikolaou S, Cui Y and Ghoniem N 2017 *Modelling Simul. Mater. Sci. Eng.* **26** 013001
[23] Yilmaz H, Williams C J and Derby B 2020 *Mater. Sci. Eng.* A **793** 139883
[24] Ustrzycka A, Skoczen B, Nowak M, Kurpaska L, Wyszkowska E and Jagielski J 2020 *Int. J. Damage Mech.* **29** 1271–305
[25] Ruiz-Moreno A and Hähner P 2018 *Mater. Des.* **145** 168–80
[26] Voyiadjis G Z and Yaghoobi M 2017 *Crystals* **7** 321
[27] Yaghoobi M and Voyiadjis G Z 2014 *Comput. Mater. Sci.* **95** 626–36
[28] Mayo M J, Siegel R W, Narayanasamy A and Nix W 1990 *J. Mater. Res.* **5** 107
[29] Sato Y, Shinzato S, Ohmura T, Hatano T and Ogata S 2020 *Nat. Commun.* **11** 4177
[30] Domínguez-Gutiérrez F, Papanikolaou S, Esfandiarpour A, Sobkowicza P and Alava M 2021 *Mater. Sci. Eng.* A **826** 141912
[31] Kurpaska L *et al* 2022 *Mater. Des.* **217** 110639
[32] Varillas J, Ocenasek J, Torner J and Alcala J 2017 *Acta Mater.* **125** 431–41
[33] Frydrych K, Dominguez-Gutierrez F J, Alava M J and Papanikolaou S 2022 Multiscale nanoindentation modeling of concentrated solid solutions: a continuum plasticity model (available at: https://doi.org/10.48550/arXiv.2206.11833)
[34] Bonny G, Castin N and Terentyev D 2013 *Modelling Simul. Mater. Sci. Eng.* **21** 085004
[35] Musiał S, Maj M, Urbański L and Nowak M 2022 *Int. J. Solids Struct.* **238** 111411
[36] Thompson A P *et al* 2022 *Comput. Phys. Commun.* **271** 108171
[37] Bei H, George E P, Hay J L and Pharr G M 2005 *Phys. Rev. Lett.* **95** 045501
[38] Pathak S and Kalidindi S R 2015 *Mater. Sci. Eng.* R **91** 1–36
[39] Stukowski A 2010 *Modelling Simul. Mater. Sci. Eng.* **18** 015012
[40] Stukowski A, Bulatov V V and Arsenlis A 2012 *Modelling Simul. Mater. Sci. Eng.* **20** 085007
[41] Kocks U and Mecking H 2003 *Prog. Mater. Sci.* **48** 171–273
[42] Tsuchida N, Tomota Y, Moriya H, Umezawa O and Nagai K 2001 *Acta Mater.* **49** 3029–38
[43] Bouaziz O 2012 *Adv. Eng. Mater.* **14** 759–61
[44] Xu R G, Song H, Leng Y and Papanikolaou S 2021 *Materials* **14** 5220

[45] Morris J R, Bei H, Pharr G M and George E P 2011 *Phys. Rev. Lett.* **106** 165502
[46] Ma Q and Clarke D 1995 *J. Mater. Res.* **10** 853–63
[47] Begau C, Hua J and Hartmaier A 2012 *J. Mech. Phys. Solids* **60** 711–22
[48] Granberg F, Nordlund K, Ullah M W, Jin K, Lu C, Bei H, Wang L M, Djurabekova F, Weber W J and Zhang Y 2016 *Phys. Rev. Lett.* **116** 135504
[49] Yang L, Chen Y, Miller J, Weber W J, Bei H and Zhang Y 2022 *Mater. Sci. Eng.* A **856** 143685
[50] Ashby M 1970 *Phil. Mag.* A **21** 399–424